Scilight

Photochemistry and Spectroscopy
https://www.sciltp.com/journals/ps

Article

Electronic Structural Analysis of the Infrared Intensity Generation and Enhancement Occurring upon Formation of the Bis(Pyridine)Iodonium Cation †

Kosuke Oyaizu [1] and Hajime Torii [1,2,*]

[1] Applied Chemistry and Biochemical Engineering Course, Department of Engineering, Graduate School of Integrated Science and Technology, Shizuoka University, 3-5-1 Johoku, Chuo-ku, Hamamatsu 432-8561, Japan
[2] Department of Optoelectronics and Nanostructure Science, Graduate School of Science and Technology, Shizuoka University, 3-5-1 Johoku, Chuo-ku, Hamamatsu 432-8561, Japan
* Correspondence: torii.hajime@shizuoka.ac.jp
† This article is dedicated to Prof. Giuseppe Zerbi in recognition of his outstanding scientific contributions to Spectroscopy.

How To Cite: Oyaizu, K.; Torii, H. Electronic Structural Analysis of the Infrared Intensity Generation and Enhancement Occurring upon Formation of the Bis(Pyridine)Iodonium Cation. *Photochemistry and Spectroscopy* **2026**, *2*(2), 6. https://doi.org/10.53941/ps.2026.100017

Received: 6 December 2025
Revised: 16 March 2026
Accepted: 19 March 2026
Published: 9 May 2026

Abstract: Behavior of electrons is often essentially important for infrared intensities of strongly infrared-active vibrational modes, and elucidating its features is helpful in deepening our understanding on the electronic structural properties of the concerned molecular systems. Here, such an analysis based on electron density features is carried out for the bis(pyridine)iodonium cation (the pyridine···I^+···pyridine complex), a representative system containing a three-center four-electron (3c4e) halogen bond. It is shown that, for the infrared intensity generation and enhancement of two vibrational modes that occur upon formation of this complex, vibration-induced partial transfer of electron density (called charge flux) plays an essential role. It is also shown that the effective electric charge of I^+ in this complex is 0.6–0.7 *e*, which is significantly less than 1 *e* of an isolated I^+ ion, suggesting that the 3c4e halogen bond of the N···I^+···N part has a partially covalent character. The extent of anisotropy in the occupancies of electrons in the *p* orbitals of the outer-most shell of I^+ is ~0.8 in the mixing ratio of $p_x^2p_y^2p_z^0$. Similarities and differences with the case of the protonated complex are also discussed.

Keywords: infrared intensity; charge flux; electron density; halogen bond; iodonium

1. Introduction

Halogen bonding is a highly directional attractive interaction between an electron-deficient region of a halogen atom and a (partially) negatively charged atom in a molecular system [1–13]. In its most widely recognized form, the halogen atom is covalently bonded to another atom (most frequently carbon atom), and the halogen bond is formed nearly on the line extended from (i.e., on the other side of) the covalent bond. The most important feature giving rise to this directionality [14–19], or to the formation of halogen bond at all, is the anisotropy in the electron distribution that is intrinsic [20,21] to the $p_x^2p_y^2p_z^1$ configuration in the outermost shell of the halogen atom, where *z* is taken along the covalent bond (with the covalent bond being placed on the $-z$ side in the following argument). This anisotropy tends to generate a spatial region of positive electrostatic potential around the $+z$ side of the *z* axis, which is called σ hole [22,23], and hence, to contribute to the formation of halogen bond in a nearly linear shape. Because the lowest-order electric moment of an isolated halogen atom in the $p_x^2p_y^2p_z^1$ electronic configuration is a quadrupole, it is in principle most natural to represent this anisotropic electrostatic situation by an electric quadrupole on the halogen atom [20,21,24–27]. In a practical sense, however, it is convenient to represent it by placing a partial positive charge at a certain distance from the halogen atom on the $+z$ side of the *z* axis, called extra-point model [28–34].

There is another form of halogen bonding known, formed by a halogen(I) ion (X^+) and two (partially) negatively charged atoms (hereafter denoted as D) [35–37]. Here, it is supposed that two of the three *p* orbitals in the outermost shell of the X^+ ion are doubly occupied and the rest (assumed as p_z in the following argument) is vacant, and one of the two D atoms is located on the $+z$ side and the other on the $-z$ side of the *z* axis to form mutually (nearly) linear two halogen bonds. Because three centers and four electrons (donated by the two D atoms) are involved, this is also known as a three-center four-electron (3c4e) halogen bond. In addition to its fundamental properties [38–41], especially its partially covalent nature [37,42–45], its useful applications in organic chemistry [46–48] and supramolecular chemistry [49–52] are frequently discussed.

One of the well-studied species in the series of 3c4e halogen-bonded systems of X^+ would be the bis(pyridine)iodonium cation (the pyridine···I^+···pyridine complex) [37,38,42–46,53]. In a previous study [53] it was observed that, upon its formation, an infrared (IR) band is newly generated at 172 cm^{-1} and was assigned to the antisymmetric stretching of the N···I^+···N part. A practical aspect of this observation would be that this band may be used as a marker of the formation of the N···I^+···N 3c4e halogen bond, but from a more basic viewpoint, it would be preferable to elucidate in the first place how this IR intensity generation takes place. Is it interpretable by a simple displacement of a charged particle (I^+ in this case), or is there any more complex mechanism operating? In our previous studies on some other halogen-bonded systems [54–56], it was clarified that IR intensity enhancement is induced for some vibrational modes by a spatially extended transfer of electron density, which is called charge flux [54–62]. If such spatially extended behavior of electrons is involved in the IR intensity generation also in the case of the bis(pyridine)iodonium cation, it is expected that it is also related to the electronic structural aspect of this cation, especially the partially covalent nature of the 3c4e halogen bond. By carefully examining the features of the IR spectrum observed in Ref. [53] by referring to those of liquid pyridine [63,64], it is also recognized that the IR intensity of the band at 638 cm^{-1}, which is assigned to the antisymmetric mixing of the 6a vibrations of the two pyridine rings (where, in each molecule, the N and *para* C atoms are displaced along the *z* axis in the opposite directions), is also enhanced in relative intensity. Elucidating the mechanism that gives rise to these IR intensity generation and enhancement would be helpful for our better understanding of the properties of the 3c4e halogen bond formed by the X^+ ions.

In the present study, this problem is tackled by performing theoretical analyses on the electron density changes occurring upon formation of the bis(pyridine)iodonium cation and their derivatives with respect to vibrational modes. By analyzing electron density features, it is possible to elucidate the behavior of electrons in intermolecular interactions and vibrational motions in a spatially resolved manner [33,34,54–56,65,66]. To support the discussion, calculations were also carried out for the pyridinium–pyridine dimer, which is a hydrogen-bonded system that has H^+ instead of I^+. Based on the results of those analyses, the electronic structural and vibrational properties of the cation will be discussed.

2. Computational Procedures

Calculations and analyses were carried out for the bis(pyridine)iodonium cation (the pyridine···I^+···pyridine complex) and its related species, focusing on the change in the electron density upon formation of this cation from its components (two pyridine molecules and the iodonium ion) and the electron density derivatives related to the two modes that appear strongly in the IR spectra upon formation of this cation. First, the structures were optimized, and the vibrational frequencies and IR intensities were calculated, with the ωB97XD functional [67] of density functional theory (DFT) and the def2SVP basis set [68,69]. No scaling was carried out on the calculated frequencies. The globally optimized structure was found to be of the D_{2d} symmetry, with linear N···I^+···N angle, equal N···I^+ distances (2.289 Å), and mutually perpendicular pyridine rings, in agreement with the results of previous calculations [37,38,42,43], although a coplanar structure of D_{2h} symmetry was suggested in a previous analysis of observed IR spectra [53]. In the following, the location of I^+ is taken as the origin, the N···I^+···N direction is taken as the *z* axis, and the ring on the $-z$ side is placed on the *yz* plane.

The change in the electron density upon formation of the bis(pyridine)iodonium cation, denoted as $\delta[\rho^{(el)}(\boldsymbol{r})]_{total}$, was calculated as $[\rho^{(el)}(\boldsymbol{r})]_{py\_I^+\_py} - [\rho^{(el)}(\boldsymbol{r})]_{I^+} - \Sigma[\rho^{(el)}(\boldsymbol{r})]_{pyridine}$, where the sum was taken over the two pyridine molecules in the third term. In addition, to support the discussion, the changes in the electron density induced by an electric charge of 0.2 *e* and a *zz* axially symmetric traceless electric quadrupole of 1 ea_0^2 located at the origin (replacing the I^+ ion), denoted as $\delta[\rho^{(el)}(\boldsymbol{r})]_{charge}$ and $\delta[\rho^{(el)}(\boldsymbol{r})]_{quad}$, were also calculated. The evaluation points $\boldsymbol{r}$ of $\rho^{(el)}(\boldsymbol{r})$ were taken in a rectangular box of the size of 14.4 × 14.4 × 22.2 $Å^3$, so that each boundary of the box is at least 5 Å from any atom in the cation, with the interval of 0.02 Å. In evaluating $[\rho^{(el)}(\boldsymbol{r})]_{I^+}$, the I^+ ion was assumed to be in the singlet state with two doubly occupied and one vacant *p* orbitals of the outermost shell. For well-founded discussion, it is required to specify which of those three *p* orbitals is vacant. For this purpose, small negative electric

charges of -1×10^{-6} *e* or less (in magnitude) were placed at *x*, *y*, or *z* = ±50 Å. These charges have a negligibly small effect on the energy but are sufficient to lift the degeneracy to make the specified *p* orbital vacant [33].

The derivative of the electron density with respect to a vibrational mode *Q* or a displacement *Z* of a specified atom, denoted as $\partial\rho^{(el)}(\boldsymbol{r})/\partial Q$ or $\partial\rho^{(el)}(\boldsymbol{r})/\partial Z$, was calculated by numerical differentiation from $\rho^{(el)}(\boldsymbol{r})$ of the equilibrium and displaced (ΔQ = 0.03 Å amu$^{1/2}$ or ΔZ = 0.02 Å) structures. The change in this electron density derivative upon formation of the bis(pyridine)iodonium cation was calculated in the same way as $\delta[\rho^{(el)}(\boldsymbol{r})]_{total}$ described above.

To support the discussion, calculations were also carried out for the pyridinium–pyridine dimer (the pyridine···H^+···pyridine complex). In this case, the globally optimized structure has the C_{2v} symmetry [38,70–73] with linear N···H^+···N angle and mutually perpendicular pyridine rings but unequal N···H^+ distances (1.128 and 1.513 Å), while the optimized structure constrained to the D_{2d} symmetry (with the N···H^+ distances of 1.283 Å) is a first-order transition state (i.e., with one imaginary-frequency mode). As a result, the electron density derivatives were calculated for both of these structures.

All the DFT calculations described above were performed by using the Gaussian 09 program [74], and the analyses (including preparation of vibrationally displaced structures, and numerical differentiation, integration, and fitting of electron densities) were done with our own programs.

3. Results and Discussion

3.1. Features of Electron Density Derivatives

As stated in Section 1, it was observed in a previous study [53] that, upon formation of the bis(pyridine)iodonium cation, a strongly IR-active band is newly generated at 172 cm^{-1}, which is assigned to the antisymmetric stretching of the N···I^+···N part. In the present calculation at the ωB97XD/def2SVP level, it is calculated at 192.8 cm^{-1} with the IR intensity of 110.1 km mol^{-1}. To elucidate the electronic structural origin of this generation of IR intensity, the electron density derivative with respect to the displacement of I^+ along the *z* axis (denoted as Z_{I+}), which is equivalent to the N···I^+···N antisymmetric stretching, is calculated. The result obtained in the form of $\delta[\partial\rho^{(el)}(\boldsymbol{r})/\partial Z_{I+}]$, defined as $[\partial\rho^{(el)}(\boldsymbol{r})/\partial Z_{I+}]_{py\_I+\_py} - [\partial\rho^{(el)}(\boldsymbol{r})/\partial Z_{I+}]_{I+}$, is shown in Figure 1a. Here, $[\partial\rho^{(el)}(\boldsymbol{r})/\partial Z_{I+}]_{I+}$ is subtracted to cancel the contribution of the electrons that simply follow the displacement of the I^+ ion. In calculating this $[\partial\rho^{(el)}(\boldsymbol{r})/\partial Z_{I+}]_{I+}$, the $p_x^2p_y^2p_z^0$ configuration in the outermost shell of I^+ is assumed. It is clearly seen that, although only the I^+ ion is displaced, the electron density changes are delocalized to the spatial region of the two pyridine molecules. In the two-dimensional plot (integrated projection on the *yz* plane), the features on the right-hand side constitute a side view of the pyridine ring placed on the *xz* plane, and indicate that both the lone-pair electrons and the π electrons on the N atom of the pyridine molecule contribute to this electron density derivative. The running integral of the one-dimensional plot shown with a light blue line indicates that, in fact, the spatial region with large amplitudes of this electron density derivative is extended to the whole part of the two pyridine rings. The positive sign of this running integral indicates that the electron density is partially transferred in the $-z$ direction (from right to left) as the I^+ ion is displaced in the $+z$ direction along the *z* axis.

Because of the spatially extended nature, this vibration-induced partial electron density transfer (called charge flux [54–62]) gives rise to a dipole derivative of as large as 12.4 D Å^{-1}. In atomic unit, this is 2.58 $(ea_0)a_0^{-1}$, meaning that it is equivalent to a displacement of a positive electric charge of 2.58 *e*. This should be further added by the contribution of $[\partial\rho^{(el)}(\boldsymbol{r})/\partial Z_{I+}]_{I+}$ and the displacement of the atomic nucleus, the sum of which is simply 1 *e*. However, this result does not mean that the effective electric charge of I^+ in the bis(pyridine)iodonium cation is 3.58 *e*. The dipole derivative is significantly anisotropic to the extent that it is as small as 0.16 *e* for the displacements in the out-of-line (*x* and *y*) directions. Stretching of one N···I^+ bond and shrinking of the other concertedly induce a large charge flux and give rise to an enhancement of ~13 (=3.58^2) times of the IR intensity.

The features in the spatial region around the I^+ ion in the two-dimensional plot shown in Figure 1a would need an additional remark. It may seem as if the positive and negative lobes in the -1 Å $< z <$ 1 Å region are related to the direction of the partial electron density transfer discussed above. In fact, the signs of these lobes are related to how we suppose the state of the I^+ ion in evaluating $[\partial\rho^{(el)}(\boldsymbol{r})/\partial Z_{I+}]_{I+}$ (which is subtracted from $[\partial\rho^{(el)}(\boldsymbol{r})/\partial Z_{I+}]_{py\_I+\_py}$ to derive $\delta[\partial\rho^{(el)}(\boldsymbol{r})/\partial Z_{I+}]$). The result obtained by assuming the average of the $p_x^2p_y^2p_z^0$, $p_y^2p_z^2p_x^0$, and $p_z^2p_x^2p_y^0$ configurations (hereafter referred to as the isotropic average configuration) in evaluating $[\partial\rho^{(el)}(\boldsymbol{r})/\partial Z_{I+}]_{I+}$ is shown in Figure 1b. It is clearly seen that the signs of the positive and negative lobes in the -1 Å $< z <$ 1 Å region are inverted. Then, it would be most reasonable to consider that the extent of anisotropy in the occupancies of electrons in the *p* orbitals of I^+ in the bis(pyridine)iodonium cation may be evaluated from the ratio of $p_x^2p_y^2p_z^0$ and isotropic average configurations (assumed in Figure 1a,b, respectively) that best cancels the features in the -1 Å $< z <$ 1 Å region. From the peak heights of the black lines of the one-dimensional plots shown in Figure 1a and b, this ratio is estimated as 0.64 (for a) to 0.36 (for b). As shown in Figure 1c, the features in the

−1 Å < z < 1 Å region are indeed mostly canceled by adopting this ratio. According to this reasoning, the ratio of mixing of the $p_x^2p_y^2p_z^0$, $p_y^2p_z^2p_x^0$, and $p_z^2p_x^2p_y^0$ configurations for I^+ in the bis(pyridine)iodonium cation is estimated as 0.76, 0.12, and 0.12, respectively.

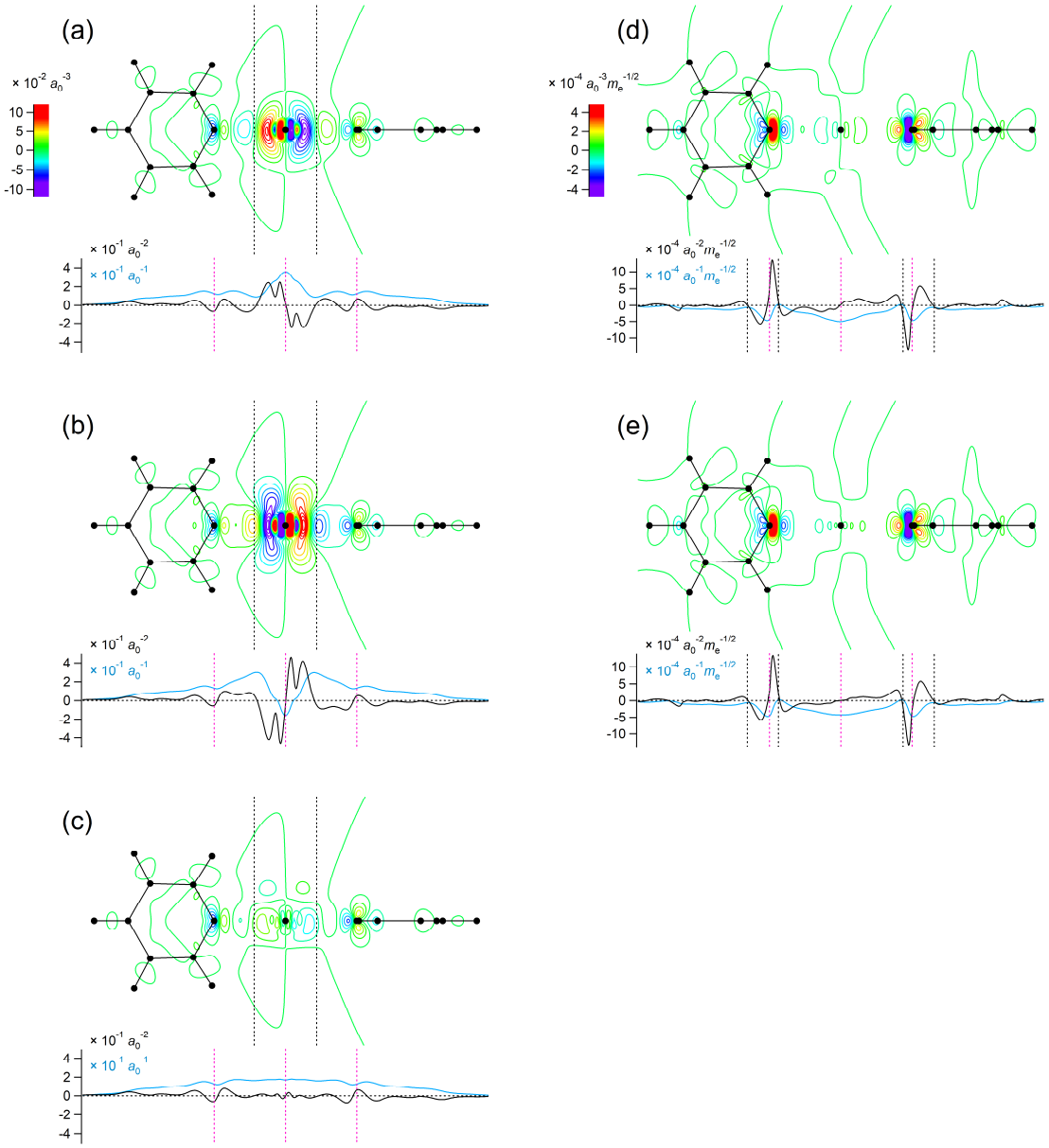

Figure 1. Two-dimensional contour plot (integrated projection on the *yz* plane), one-dimensional plot (integrated projection on the *z* axis, black), and its left-to-right running integral (light blue) of the change in the electron density derivatives $\delta[\partial\rho^{(el)}(\boldsymbol{r})/\partial Z_{I+}]$ ($\equiv[\partial\rho^{(el)}(\boldsymbol{r})/\partial Z_{I+}]_{py\_I+\_py} - [\partial\rho^{(el)}(\boldsymbol{r})/\partial Z_{I+}]_{I+}$, in panels **a**–**c**) and $\delta[\partial\rho^{(el)}(\boldsymbol{r})/\partial Q_{14}]$ ($\equiv[\partial\rho^{(el)}(\boldsymbol{r})/\partial Q_{14}]_{py\_I+\_py} - [\partial\rho^{(el)}(\boldsymbol{r})/\partial Q_{14}]_{I+} - \Sigma[\partial\rho^{(el)}(\boldsymbol{r})/\partial Q_{14}]_{pyridine}$, in panels **d** and **e**) occurring upon formation of the bis(pyridine)iodonium cation, where Z_{I+} represents the displacement of I^+ along the *z* axis and Q_{14} denotes the 14th normal mode (655.9 cm^{-1}), calculated at the ωB97XD/def2SVP level. The N···I^+···N direction is taken as the *z* (horizontal) axis, and the ring on the left-hand side is placed on the *yz* plane. In calculating $[\partial\rho^{(el)}(\boldsymbol{r})/\partial Z_{I+}]_{I+}$ and $[\partial\rho^{(el)}(\boldsymbol{r})/\partial Q_{14}]_{I+}$, the $p_x^2p_y^2p_z^0$ configuration in the outermost shell of I^+ is assumed in panels **a** and **d**, and the isotropic average configuration in panels **b** and **e**. In panel **c**, the mixing of the $p_x^2p_y^2p_z^0$, $p_y^2p_z^2p_x^0$, and $p_z^2p_x^2p_y^0$ configurations with the ratio of 0.76, 0.12, and 0.12 (see text) is assumed. The contours are drawn with the interval of 1.4×10^{-2} a_0^{-3} in the range from −35 to 35×10^{-2} a_0^{-3} (in panels **a**–**c**) and with the interval of 0.6×10^{-4} a_0^{-3} $m_e^{-1/2}$ in the range from −15 to 15×10^{-4} a_0^{-3} $m_e^{-1/2}$ (in panels **d** and **e**), with the color code shown on the left-hand side of panels **a** and **d**. The locations of the atoms are indicated with black filled circles in the two-dimensional plot, and those of the N atoms and the I^+ ion (at z = ±2.289 and 0 Å) with pink dotted lines in the one-dimensional plot. As the guide to the eye, the locations of z = ±1 Å (see text) are indicated in the two-dimensional plots of panels **a**–**c**, and those of z = ±2 and ±3 Å (see text) are indicated in the one-dimensional plots of panels **d** and **e**, with black dotted lines.

Upon formation of the bis(pyridine)iodonium cation, the IR band at 638 cm^{-1}, which is assigned to the antisymmetric mixing of the 6a vibrations of the two pyridine rings, is also enhanced in relative intensity [53] (i.e., relatively to the nearby strong IR band at ~700 cm^{-1} assigned to mode 11) compared with the band of the same mode observed at 604 cm^{-1} in the IR spectrum of liquid pyridine [63,64]. In the present calculation at the ωB97XD/def2SVP level, it is calculated at 655.9 cm^{-1} with the IR intensity of 67.1 km mol^{-1}. Compared with the IR intensity of 4.7 km mol^{-1} of this mode (at 615.2 cm^{-1}) of an isolated pyridine molecule calculated at the same theoretical level, the IR intensity is indeed significantly enhanced upon formation of the bis(pyridine)iodonium cation. The electron density derivative with regard to this mode (the 14th mode counted from the lowest frequency and hereafter denoted as Q_{14}) obtained in the form of $\delta[\partial\rho^{(el)}(\boldsymbol{r})/\partial Q_{14}]$, defined as $[\partial\rho^{(el)}(\boldsymbol{r})/\partial Q_{14}]_{py\_I^+\_py} - [\partial\rho^{(el)}(\boldsymbol{r})/\partial Q_{14}]_{I^+} - \Sigma[\partial\rho^{(el)}(\boldsymbol{r})/\partial Q_{14}]_{pyridine}$, is shown in Figure 1d,e. Here, the signs of the 6a vibrations of the two pyridine rings in their antisymmetric mixing in Q_{14} are set in a way that the two N atoms are displaced in the $+z$ direction (and, concomitantly, the two C atoms in the *para* position are displaced in the $-z$ direction) for $Q_{14} > 0$. In contrast to the case of $\delta[\partial\rho^{(el)}(\boldsymbol{r})/\partial Z_{I^+}]$ discussed above, because the vibrational amplitude of I^+ is very small, the features of this electron density derivative are essentially the same whether the state of the I^+ ion in evaluating $[\partial\rho^{(el)}(\boldsymbol{r})/\partial Q_{14}]_{I^+}$ is assumed as $p_x^2p_y^2p_z^0$ (shown in panel d) or the isotropic average (shown in panel e).

In the two-dimensional plot shown in the upper part of Figure 1d (or 1e), large amplitudes of the electron density derivative are clearly recognized around the two N atoms. In the one-dimensional plot shown in black in the lower part, each of these features in the -3 Å $< z < -2$ Å and 2 Å $< z <$ 3 Å regions appears as a combination of a high (or deep) peak and two lower side peaks of the opposite sign, and because the outer one (i.e., at a larger $|z|$) of the side peaks has a larger amplitude than the inner one, it gives rise to a dipole derivative in the $-z$ direction. However, from the running integral of the one-dimensional plot shown in light blue, it is noticed that the partial electron density transfer induced by this vibrational mode is spatially much more extended, i.e., an extended charge flux is generated. This running integral is negative over almost the whole range, including the spatial regions of the two pyridine rings, and as a result, a large dipole derivative is induced in the $-z$ direction. It amounts to −0.838 D $Å^{-1}$ $amu^{-1/2}$, which constitutes a major part of the total dipole derivative of −1.260 D $Å^{-1}$ $amu^{-1/2}$ (corresponding to the IR intensity of 67.1 km mol^{-1}) of this vibrational mode.

Therefore, it is concluded that a large charge flux extended over the whole spatial region of the bis(pyridine)iodonium cation plays an important role in the IR intensity generation and enhancement of the two vibrational modes calculated at 192.8 and 655.9 cm^{-1}.

3.2. Electronic Anisotropy of I^+ and Polarization of Pyridine Molecules

The change in the electron density $\delta[\rho^{(el)}(\boldsymbol{r})]_{total}$ occurring upon formation of the bis(pyridine)iodonium cation, defined (as described in Section 2) as $[\rho^{(el)}(\boldsymbol{r})]_{py\_I^+\_py} - [\rho^{(el)}(\boldsymbol{r})]_{I^+} - \Sigma[\rho^{(el)}(\boldsymbol{r})]_{pyridine}$, is shown in Figure 2a–d. The state of the I^+ ion in evaluating $[\rho^{(el)}(\boldsymbol{r})]_{I^+}$ is assumed as $p_x^2p_y^2p_z^0$ in panel a and as the isotropic average in panel b. It is (rather naturally) recognized that the features around the center (-1.5 Å $< z <$ 1.5 Å) depend strongly on how we suppose the state of the I^+ ion in evaluating $[\rho^{(el)}(\boldsymbol{r})]_{I^+}$; negative lobes are clearly recognizable along the y axis at $z = 0$ and positive lobes are prominent at $(y, z) = (0, \pm 1.0)$ Å when we suppose the $p_x^2p_y^2p_z^0$ configuration, while positive lobes are present with large amplitudes along the y axis at $z = 0$ and smaller but clear negative lobes are seen at $(y, z) = (0, \pm 0.86)$ Å when we suppose the isotropic average configuration. For the electron density derivatives shown in Figure 1a–c, it has been discussed in Section 3.1 that the features around the center are mostly canceled by mixing the three configurations with the ratio of 0.76, 0.12, and 0.12. However, by applying this ratio in calculating $\delta[\rho^{(el)}(\boldsymbol{r})]_{total}$, clearly recognizable positive lobes remain along the y axis as shown in Figure 2c, so that the anisotropy of the electron distribution in I^+ that is effective in $\delta[\rho^{(el)}(\boldsymbol{r})]_{total}$ looks more or less different (discussed later in this section, by referring also to Figure 2d).

In Figure 2a–d, the electron density changes are also recognized in the spatial regions of the two pyridine rings. The running integral (light blue line) is negative over the spatial region of the pyridine ring on the left-hand ($z < 0$) side and vice versa on the right-hand ($z > 0$) side, meaning that electron density is partially transferred from the outer part to the inner part, inducing an electric polarization in the outward direction on each (right- and left-hand) side.

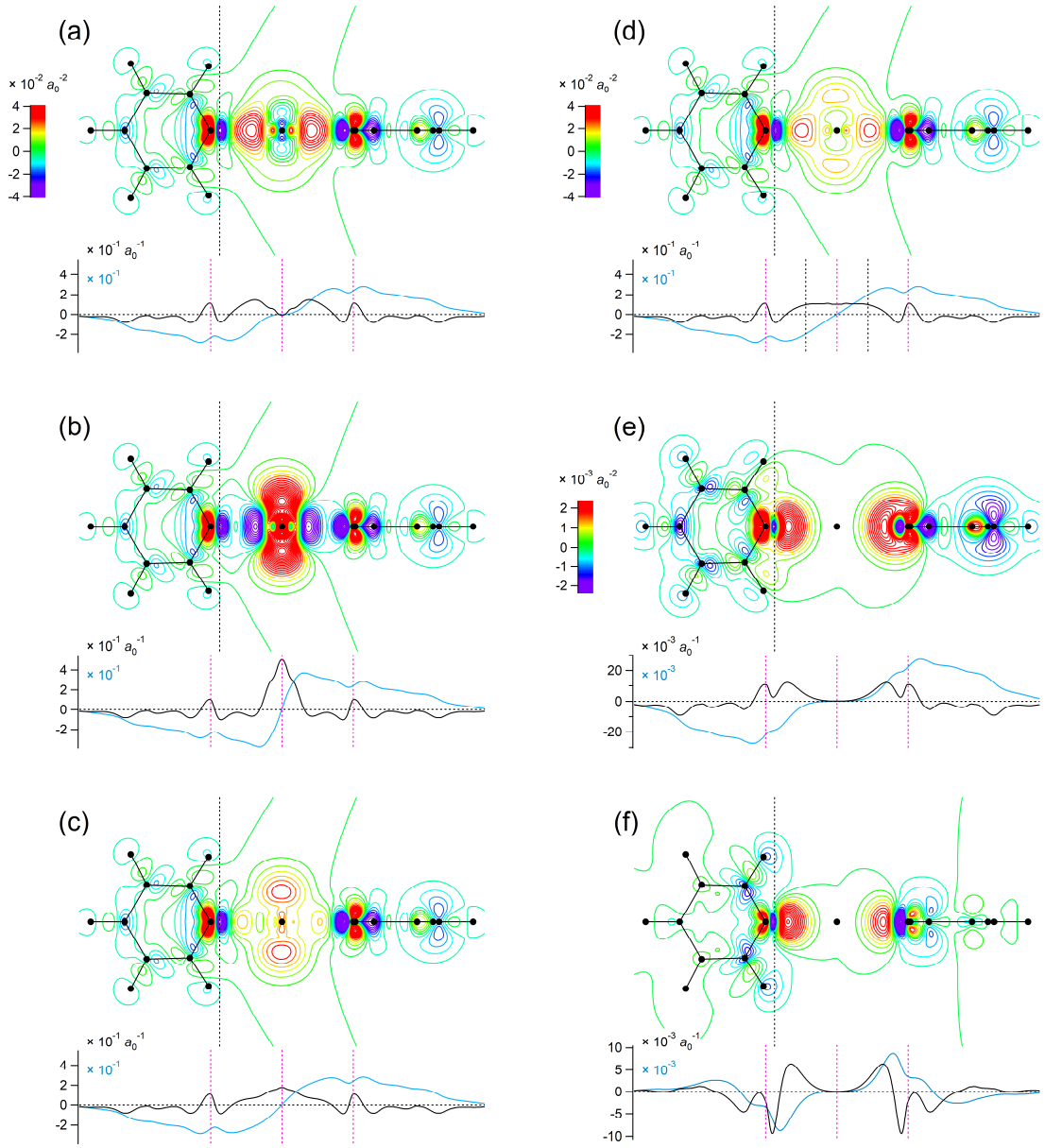

Figure 2. (**a**–**d**) Two-dimensional contour plot (integrated projection on the *yz* plane), one-dimensional plot (integrated projection on the *z* axis, black), and its left-to-right running integral (light blue) of the change in the electron density $\delta[\rho^{(el)}(\boldsymbol{r})]_{total}$ ($\equiv[\rho^{(el)}(\boldsymbol{r})]_{py\_I^+\_py} - [\rho^{(el)}(\boldsymbol{r})]_{I^+} - \Sigma[\rho^{(el)}(\boldsymbol{r})]_{pyridine}$) occurring upon formation of the bis(pyridine)iodonium cation calculated at the ωB97XD/def2SVP level. The location of I^+ is taken as the origin, the N···I^+···N direction is taken as the *z* (horizontal) axis, and the ring on the left-hand side is placed on the *yz* plane. In calculating $[\rho^{(el)}(\boldsymbol{r})]_{I^+}$, the $p_x^2p_y^2p_z^0$ configuration in the outermost shell of I^+ is assumed in panel **a**, the isotropic average configuration in panel **b**, and the $p_x^2p_y^2p_z^0$, $p_y^2p_z^2p_x^0$, and $p_z^2p_x^2p_y^0$ configurations are mixed with the ratio of 0.76, 0.12, and 0.12 in panel **c** and with the ratio of 0.86, 0.07, and 0.07 in panel **d**. The contours are drawn with the interval of 0.48 × 10^{-2} a_0^{-2} in the range from −12 to 12 × 10^{-2} a_0^{-2}, with the color code shown on the left-hand side of panel **a** and **d**. The locations of the atoms are indicated with black filled circles in the two-dimensional plot, and those of the N atoms and the I^+ ion with pink dotted lines in the one-dimensional plot. As the guide to the eye, the location of $z = -2$ Å (see text) is indicated in each two-dimensional plot, and the locations of $z = \pm1$ Å (see text) are indicated in the one-dimensional plot of panel **d**, with black dotted lines. (**e**,**f**) The same type of plots of the change in the electron density $\delta[\rho^{(el)}(\boldsymbol{r})]_{charge}$ and $\delta[\rho^{(el)}(\boldsymbol{r})]_{quad}$ induced by an electric charge of 0.2 *e* (panel **e**) and a *zz* axially symmetric traceless electric quadrupole of 1 ea_0^2 (panel **f**) located at the origin (replacing the I^+ ion). The locations and the structures of the two pyridine molecules are the same as those in the bis(pyridine)iodonium cation. The contours are drawn with the interval of 0.3 × 10^{-3} a_0^{-2} in the range from −7.5 to 7.5 × 10^{-3} a_0^{-2}, with the color code shown on the left-hand side of panel **e**.

To help examine the nature of this polarization in more detail, the electron density changes induced by an electric charge of 0.2 *e* and a *zz* axially symmetric traceless electric quadrupole of 1 ea_0^2 located at the origin (replacing the I^+ ion), denoted as $\delta[\rho^{(el)}(\boldsymbol{r})]_{charge}$ and $\delta[\rho^{(el)}(\boldsymbol{r})]_{quad}$, are calculated. The results are shown in Figure 2e and f. It is seen that the spatial regions with large amplitudes of electron density change are extended to the far end of the pyridine rings in the polarization induced by an electric charge shown in Figure 2e, while it is shorter-ranged and rather localized around the N and *ortho* C atoms in the polarization induced by an electric quadrupole shown in Figure 2f. The feature of the electron density change $\delta[\rho^{(el)}(\boldsymbol{r})]_{total}$ that occurs in the real cation shown in Figure 2a–d seems to be in between those of the two types of electrostatic polarizations. Therefore, we have tried to fit $\delta[\rho^{(el)}(\boldsymbol{r})]_{total}$ shown in Figure 2b by a linear combination of $\delta[\rho^{(el)}(\boldsymbol{r})]_{charge}$ and $\delta[\rho^{(el)}(\boldsymbol{r})]_{quad}$, by minimizing the integral of $(\delta[\rho^{(el)}(\boldsymbol{r})]_{total} - c_1\,\delta[\rho^{(el)}(\boldsymbol{r})]_{charge} - c_2\,\delta[\rho^{(el)}(\boldsymbol{r})]_{quad})^2$, in the $z < -2$ Å (or its symmetrically related $z > 2$ Å) region. The values of c_1 and c_2 obtained in this way are $c_1 = 8.643$ and $c_2 = 6.013$. The one- and two-dimensional plots of $\delta[\rho^{(el)}(\boldsymbol{r})]_{total} - c_1\,\delta[\rho^{(el)}(\boldsymbol{r})]_{charge} - c_2\,\delta[\rho^{(el)}(\boldsymbol{r})]_{quad}$ using these values of c_1 and c_2 (hereafter denoted as $\delta[\rho^{(el)}(\boldsymbol{r})]_{residual}$), which are shown in Figure 3a, clearly indicate that $\delta[\rho^{(el)}(\boldsymbol{r})]_{total}$ is reasonably well fitted by $c_1\,\delta[\rho^{(el)}(\boldsymbol{r})]_{charge} + c_2\,\delta[\rho^{(el)}(\boldsymbol{r})]_{quad}$ in the $z < -2$ Å and $z > 2$ Å regions. However, the effective electric charge and quadrupole of I^+ in the cation estimated by these values, 1.729 *e* and 6.013 ea_0^2, seem to be too large compared with 1.0 *e* and 4.847 ea_0^2 of an isolated I^+ ion of the $p_x^2p_y^2p_z^0$ configuration.

The features of $\delta[\rho^{(el)}(\boldsymbol{r})]_{residual}$ around the center are considered to provide us information on the state of I^+ in the cation. As a reference, the electron density difference between the $p_x^2p_y^2p_z^0$ and isotropic average configurations of an isolated I^+ ion is shown in Figure 3b. Compared to this, each positive lobe ($y > 0$ and $y < 0$) along the *y* axis at $z = 0$ in $\delta[\rho^{(el)}(\boldsymbol{r})]_{residual}$ shown in Figure 3a has a similar shape and amplitude, but each negative lobe ($z > 0$ and $z < 0$) along the *z* axis at $y = 0$ looks double peaked and is somewhat more extended to the spatial region around the N atom. The latter feature originates from the positive lobes sticking out (in the $|z| < 2$ Å region) from the N atoms in the electron density changes due to electrostatic polarizations $\delta[\rho^{(el)}(\boldsymbol{r})]_{charge}$ and $\delta[\rho^{(el)}(\boldsymbol{r})]_{quad}$ shown in Figure 2e,f, which are considered to be suppressed in the real cation because of the existence of I^+ at the center. To make the situation clearer, the difference between the electron densities shown in Figure 3a,b is plotted in Figure 3c. It is recognized that electron density is partially transferred in the N → I^+ direction from $|z| \sim 1.7$ Å to ~0.8 Å within each N···I^+ halogen bond, with the magnitude estimated as ~0.15 (i.e., corresponding to an electric charge of ~0.15 *e*) from the amplitude of the running integral. In contrast, along the *y* axis at $z = 0$, the amplitude of $\delta[\rho^{(el)}(\boldsymbol{r})]_{residual}$ is only slightly smaller by a factor of ~0.9 (at $|y| \sim 0.75$ Å) than that of I^+ in the $p_x^2p_y^2p_z^0$ configuration. Because of this extended nature of $\delta[\rho^{(el)}(\boldsymbol{r})]_{residual}$ along the *z* axis, the *zz* component of the electric quadrupole corresponding to $\delta[\rho^{(el)}(\boldsymbol{r})]_{residual}$ in the -2 Å $< z < 2$ Å region is calculated to be as large as 7.1 ea_0^2. This may be the reason for the abovementioned enhanced electric quadrupole (6.013 ea_0^2) that is effective in the polarization of the pyridine rings in the cation. In contrast, for the enhanced effective electric charge (1.729 *e*), there is no quantitative reasoning at present. It might be that the deshielding of the electron density around the N atoms due to N → I^+ partial transfer is responsible for it.

Following the idea adopted in Section 3.1 for estimating the extent of anisotropy in the occupancies of electrons in the *p* orbitals of I^+ in the cation, the mixing ratio of the $p_x^2p_y^2p_z^0$, $p_y^2p_z^2p_x^0$, and $p_z^2p_x^2p_y^0$ configurations is derived so that the one-dimensional plot of $\delta[\rho^{(el)}(\boldsymbol{r})]_{total}$ becomes essentially flat around the center. The plots of $\delta[\rho^{(el)}(\boldsymbol{r})]_{total}$ calculated in this way, with the mixing ratio of 0.86, 0.07, and 0.07, are shown in Figure 2d. Then, integrating it in the -1 Å $< z < 1$ Å region, the amount of excess electron density around I^+ in the cation is estimated as ~0.4, roughly in accord with the extent of partial electron density transfer estimated above from the features of $\delta[\rho^{(el)}(\boldsymbol{r})]_{residual}$, which is ~0.15 per N···I^+ halogen bond. Therefore, it would be most reasonable to consider that the effective electric charge of I^+ in the cation is 0.6–0.7 *e*, and the extent of anisotropy in the occupancies of electrons in the *p* orbitals is ~0.8 in the mixing ratio of $p_x^2p_y^2p_z^0$. The former is slightly larger than the value of 0.41 and 0.43 *e* obtained from natural population analyses in previous studies [39,43], but its qualitative implication is the same in that the 3c4e halogen bond of the N···I^+···N part has a partially covalent character. With regard to the effects of the electric charge and quadrupole of I^+ on the polarization of pyridine rings, however, the effective values are much larger because of some extent of redistribution of electron density.

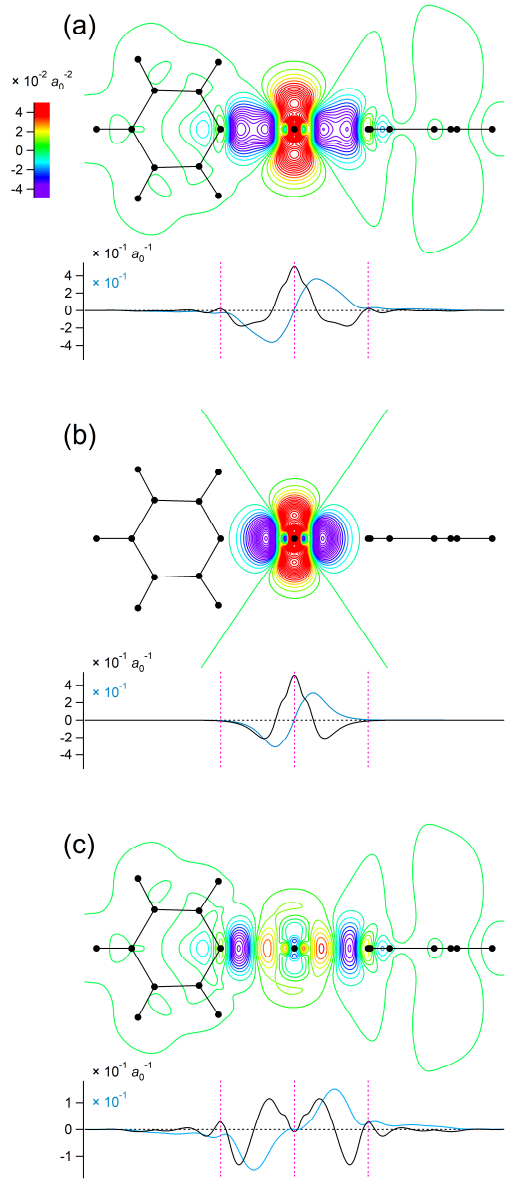

Figure 3. (**a**) Two-dimensional contour plot (integrated projection on the *yz* plane), one-dimensional plot (integrated projection on the *z* axis, black), and its left-to-right running integral (light blue) of the difference taken as $\delta[\rho^{(el)}(\boldsymbol{r})]_{total} - c_1\,\delta[\rho^{(el)}(\boldsymbol{r})]_{charge} - c_2\,\delta[\rho^{(el)}(\boldsymbol{r})]_{quad}$ that best cancels the amplitudes in the $z < -2$ Å and $z > 2$ Å regions. In calculating $\delta[\rho^{(el)}(\boldsymbol{r})]_{total}$, the isotropic average configuration in the outermost shell of I^+ is assumed (shown in Figure 2b). The contours are drawn with the interval of $0.6 \times 10^{-2}\ a_0^{-2}$ in the range from −15 to $15 \times 10^{-2}\ a_0^{-2}$, with the color code shown on the left-hand side. (**b**,**c**) The same type of plots of the difference in the electron density between the $p_x^2p_y^2p_z^0$ and isotropic average configurations in the outermost shell of an isolated I^+ ion (in panel **b**), and of the difference between the electron densities shown in panels **a** and **b** (in panel **c**). The contours are drawn with the same setting as in panel a.

3.3. The Case of H^+ Bridging Pyridine Molecules

To deepen understanding on the results discussed above for the bis(pyridine)iodonium cation, calculations and analyses have also been carried out for the pyridinium–pyridine dimer (the pyridine···H^+···pyridine complex). The one- and two-dimensional plots of the electron density derivative $[\partial\rho^{(el)}(\boldsymbol{r})/\partial Z_{H^+}]_{py\_H^+\_py}$ with respect to the displacement of H^+ along the *z* axis (denoted as Z_{H^+}) calculated for the structure of D_{2d} symmetry are shown in Figure 4a. (Here, $[\partial\rho^{(el)}(\boldsymbol{r})/\partial Z_{H^+}]_{H^+}$ is not subtracted because there is no electron around an isolated H^+.) The most conspicuous feature would be the positive and negative lobes in the $+z$ and $-z$ sides, respectively, around the center, so that it might seem as if the partial electron density transfer in the $+z$ direction is the most important. However, the running integral of the one-dimensional plot shown in light blue is positive over almost the whole range, clearly

indicating that a larger partial electron density transfer (i.e., charge flux) occurs in the −*z* direction. The positive and negative lobes around the center originate from the electrons that simply follow the displacement of H^+. Although there is no electron around an isolated H^+, some electron density is partially donated from the pyridine rings, giving rise to the feature seen around the center. As a reference, the same type of plots obtained for an isolated electrically neutral H atom is shown in Figure 4c. Comparing the depth of the dip around the center of the running integral in Figure 4a,c, the integrated electron density donated by the pyridine rings is estimated to be ~0.56, meaning that the effective electric charge of H^+ in this complex is ~0.44 *e*. In the case of the bis(pyridine)iodonium cation, the discussion in this regard developed in Section 3.1 was much more complicated because of the intrinsic anisotropy in the electron density of an isolated I^+ ion of a particular occupancy of *p* orbitals.

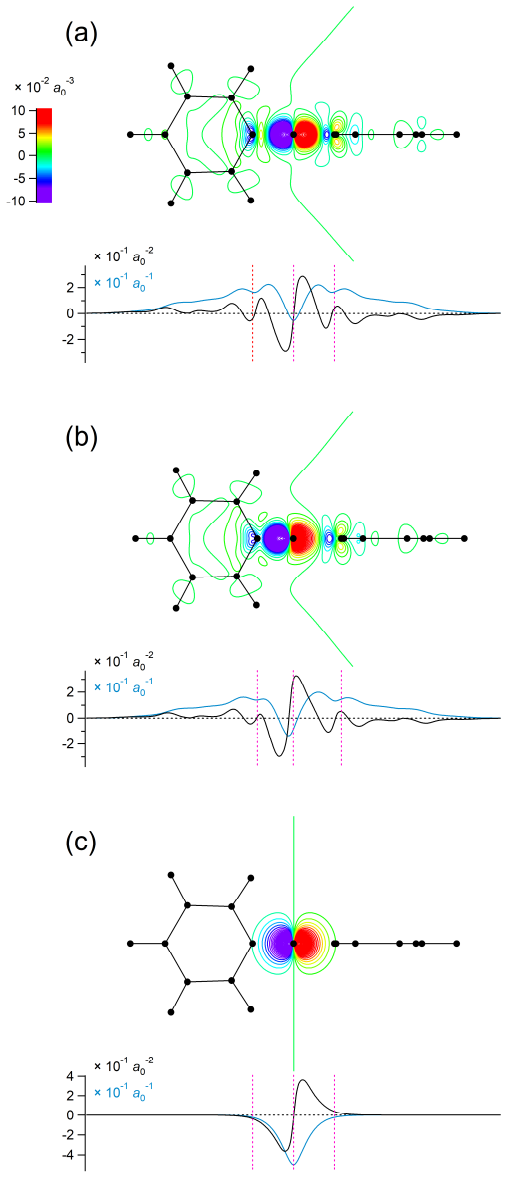

Figure 4. (**a**,**b**) Two-dimensional contour plot (integrated projection on the *yz* plane), one-dimensional plot (integrated projection on the *z* axis, black), and its left-to-right running integral (light blue) of the electron density derivative $[\partial\rho^{(el)}(\boldsymbol{r})/\partial Z_{H+}]_{py\_H+\_py}$ of the pyridinium–pyridine dimer with the symmetric location of H^+ (panel **a**) and in the equilibrium structure (panel **b**), where Z_{H+} represents the displacement of H^+ along the *z* axis, calculated at the ωB97XD/def2SVP level. The N···H^+···N direction is taken as the *z* (horizontal) axis, and the ring on the left-hand side is placed on the *yz* plane. The contours are drawn with the interval of 1.2×10^{-2} a_0^{-3} in the range from −30 to 30×10^{-2} a_0^{-3}, with the color code shown on the left-hand side of panel **a**. The locations of the atoms are indicated with black filled circles in the two-dimensional plot, and those of the N atoms and the H^+ ion with pink dotted lines in the one-dimensional plot. (**c**) The same type of plots for the displacement of a hydrogen atom located at the center. The contours are drawn with the same setting as in panel **a** and **b**.

The spatially extended charge flux described above gives rise to a dipole derivative of as large as 9.83 D Å^{-1}, or 2.05 (ea_0)a_0^{-1} in atomic unit. This should be further added by the contribution of the displacement of the atomic nucleus, which is simply 1 *e*. As a result, the total dipole derivative is equivalent to a displacement of a positive electric charge of 3.05 *e*, but similarly to the case of the bis(pyridine)iodonium cation, this should not be regarded as an effective electric charge of H^+ in the pyridinium–pyridine dimer; the dipole derivative is strongly anisotropic so that the value for the out-of-line displacements (i.e., in the *x* and *y* directions) is as small as 0.13 *e*. The similarity in the magnitude and anisotropy of the dipole derivative tensor between the two cases suggests that the situation of I^+ in the bis(pyridine)iodonium cation is quite similar to that of H^+ in the pyridinium–pyridine dimer in this regard.

As stated in Section 2, the structure of D_{2d} symmetry of the pyridinium–pyridine dimer is a first-order transition state. The mode of an imaginary frequency calculated as 679.8 *i* cm^{-1} mainly consists of the N···H$^+$···N antisymmetric stretching. The IR intensity is calculated as 8128.9 km mol^{-1}, which is in accord with the dipole derivative of 3.05 (ea_0)a_0^{-1} of the N···H$^+$···N antisymmetric stretching internal coordinate and the reduced mass of the normal mode of approximately 1 amu. In the case of the bis(pyridine)iodonium cation, the N···I$^+$···N antisymmetric stretching mode calculated at 192.8 cm^{-1} has the IR intensity of 110.1 km mol^{-1} as stated in Section 3.1, which is about 74 times smaller than the N···H$^+$···N antisymmetric stretching mode of the pyridinium–pyridine dimer. The main factor of this smaller IR intensity would be the heavier mass of the iodine atom (126.9 amu), whose effect is partially cancelled by the larger dipole derivative [3.58 vs. 3.05 (ea_0)a_0^{-1}], considering that the IR intensity is proportional to the square of the dipole derivative. Note that, in the real atomic displacements in the N···I$^+$···N antisymmetric stretching normal mode, the I^+ ion and the pyridine rings move concertedly, because pyridine is lighter than iodine.

The feature of the electron density derivative $[\partial\rho^{(el)}(\boldsymbol{r})/\partial Z_{H+}]_{py\_H+\_py}$ is quite similar also for the structure of C_{2v} symmetry at the global minimum, as shown in Figure 4b; the positive and negative lobes in the $+z$ and $-z$ sides, respectively, around the center are conspicuous, but the running integral of the one-dimensional plot is positive over almost the whole range, indicating that a larger partial electron density transfer (i.e., charge flux) occurs in the $-z$ direction. The dipole derivative induced by this charge flux is slightly smaller, 7.57 D Å^{-1} or 1.58 (ea_0)a_0^{-1} in atomic unit. This is still larger than a typical value of the OH stretching mode of strongly hydrogen-bonded water molecules, which is ~5 D Å^{-1} amu$^{-1/2}$ [65]. (Note that the reduced mass of the OH stretching normal mode is approximately 1 amu.) In the latter case also, a charge flux that is extended to the spatial region of the hydrogen-bond acceptor is the major factor of the dipole derivative; for non-hydrogen-bonded molecules, where there is no such charge flux, the dipole derivative is as small as ~1 D Å^{-1} amu$^{-1/2}$ [65]. These results emphasize the importance of charge flux in generation and enhancement of the IR intensities of strongly IR active modes.

4. Concluding Remarks

In the present study, focusing on the case of the bis(pyridine)iodonium cation, a representative system containing a three-center four-electron (3c4e) halogen bond, the behavior of electrons in the formation of this cation and in the resultant IR intensity generation and enhancement of vibrational modes has been examined by calculating and analyzing electron density features. The main conclusions may be summarized as follows. (1) For the IR intensity generation of the antisymmetric stretching vibration of the N···I$^+$···N part, which appears at 192.8 cm^{-1} with the IR intensity of 110.1 km mol^{-1}, a spatially extended charge flux plays a crucial role. It is so long ranged, being extended to the whole part of the two pyridine rings, that the dipole derivative induced by it is as large as 2.58 (ea_0)a_0^{-1}, resulting in an enhancement of ~13 [=$(2.58 + 1)^2$] times of the IR intensity compared with the case of a simple displacement of a positive charge of 1 *e*. (2) The same type of spatially extended charge flux is generated by the mode consisting of the antisymmetric mixing of the 6a vibrations of the two pyridine rings (denoted as Q_{14}), and also in the case of the pyridinium–pyridine dimer (the protonated counterpart) by the antisymmetric stretching of the N···H$^+$···N part. In the latter case, mainly because of the lighter mass of H^+ compared to I^+, the generated IR intensity is as large as 8.1×10^3 km mol^{-1}. (3) From the electron density features, the effective electric charge of I^+ in the cation is estimated as 0.6–0.7 *e*, and the extent of anisotropy in the occupancies of electrons in the *p* orbitals of the outer-most shell is estimated as ~0.8 in the mixing ratio of $p_x^2p_y^2p_z^0$. The former indicates that the 3c4e halogen bond of the N···I$^+$···N part has a partially covalent character. (4) With regard to the effects of the electric charge and quadrupole of I^+ on the polarization of pyridine rings, the effective values are much larger, estimated as 1.729 *e* and 6.013 ea_0^2, because of some extent of redistribution of electron density.

Having concluded that essentially the same type of charge flux is induced in the 3c4e halogen- and hydrogen-bonded systems by the motions of I^+ and H^+ bridging two electronegative atoms, it would be rather natural to expect that it is possible to achieve a uniform understanding of the electronic structural properties related to the dynamics of halogen(I) ions and protons interacting with surroundings. For example, it is well known that there is

an extremely broad feature in the mid-IR region of the IR spectra of acidic water called proton continuum [75,76], and one of the representative configurations supposed for hydrated protons is the Zundel complex $H_2O\cdots H^+\cdots OH_2$ [77], where H^+ bridges two electronegative atoms via hydrogen bonding. Intricate coupling between the behavior of electrons and the dynamics of ions interacting with surroundings via halogen- and hydrogen-bonding would deserve further studies.

Authors Contributions

K.O.: Investigation, Formal Analysis, Data Curation. H.T.: Conceptualization, Methodology, Software, Resources, Funding acquisition, Investigation, Formal Analysis, Data Curation, Supervision, Writing—original draft, Writing—Review & Editing. All authors have read and agreed to the published version of the manuscript.

Funding

This study was supported by JSPS KAKENHI Grant Number JP22K05020.

Institutional Review Board Statement

Not applicable.

Informed Consent Statement

Not applicable.

Data Availability Statement

Data will be made available on request.

Conflicts of Interest

The authors declare no conflict of interest.

Use of AI and AI-Assisted Technologies

No AI tools were utilized for this paper.

References

1. Desiraju, G.R.; Ho, P.S.; Kloo, L.; et al. Definition of the Halogen Bond (IUPAC Recommendations 2013). *Pure Appl. Chem.* **2013**, *85*, 1711–1713.
2. Cavallo, G.; Metrangolo, P.; Milani, R.; et al. The Halogen Bond. *Chem. Rev.* **2016**, *116*, 2478–2601.
3. Metrangolo, P.; Neukirch, H.; Pilati, T.; et al. Halogen Bonding Based Recognition Processes: A World Parallel to Hydrogen Bonding. *Acc. Chem. Res.* **2005**, *38*, 386–395.
4. Costa, P.J. The Halogen Bond: Nature and Applications. *Phys. Sci. Rev.* **2017**, *2*, 20170136.
5. Scheiner, S. Understanding Noncovalent Bonds and Their Controlling Forces. *J. Chem. Phys.* **2020**, *153*, 140901.
6. Brammer, L.; Peuronen, A.; Roseveare, T.M. Halogen Bonds, Chalcogen Bonds, Pnictogen Bonds, Tetrel Bonds and Other σ-Hole Interactions: A Snapshot of Current Progress. *Acta Crystallogr. C* **2023**, *79*, 204–216.
7. Auffinger, P.; Hays, F.A.; Westhof, E.; et al. Halogen Bonds in Biological Molecules. *Proc. Natl. Acad. Sci. USA* **2004**, *101*, 16789–16794.
8. Lu, Y.; Wang, Y.; Zhu, W. Nonbonding Interactions of Organic Halogens in Biological Systems: Implications for Drug Discovery and Biomolecular Design. *Phys. Chem. Chem. Phys.* **2010**, *12*, 4543–4551.
9. Wilcken, R.; Zimmermann, M.O.; Lange, A.; et al. Principles and Applications of Halogen Bonding in Medicinal Chemistry and Chemical Biology. *J. Med. Chem.* **2013**, *56*, 1363–1388.
10. Mukherjee, A.; Tothadi, S.; Desiraju, G.R. Halogen Bonds in Crystal Engineering: Like Hydrogen Bonds Yet Different. *Acc. Chem. Res.* **2014**, *47*, 2514–2524.
11. Gilday, L.C.; Robinson, S.W.; Barendt, T.A.; et al. Halogen Bonding in Supramolecular Chemistry. *Chem. Rev.* **2015**, *115*, 7118–7195.
12. Bulfield, D.; Huber, S.M. Halogen Bonding in Organic Synthesis and Organocatalysis. *Chem. Eur. J.* **2016**, *22*, 14434–14450.
13. Řezáč, J.; de la Lande, A. On the Role of Charge Transfer in Halogen Bonding. *Phys. Chem. Chem. Phys.* **2017**, *19*, 791–803.

14. Ramasubbu, N.; Parthasarathy, R.; Murray-Rust, P. Angular Preferences of Intermolecular Forces around Halogen Centers: Preferred Directions of Approach of Electrophiles and Nucleophiles around the Carbon-Halogen Bond. *J. Am. Chem. Soc.* **1986**, *108*, 4308–4314.
15. Lommerse, J.P.M.; Stone, A.J.; Taylor, R.; et al. The Nature and Geometry of Intermolecular Interactions between Halogens and Oxygen or Nitrogen. *J. Am. Chem. Soc.* **1996**, *118*, 3108–3116.
16. Politzer, P.; Murray, J.S.; Clark, T. Halogen Bonding: An Electrostatically-Driven Highly Directional Noncovalent Interaction. *Phys. Chem. Chem. Phys.* **2010**, *12*, 7748–7757.
17. Shields, Z.P.; Murray, J.S.; Politzer, P. Directional Tendencies of Halogen and Hydrogen Bonds. *Int. J. Quantum Chem.* **2010**, *110*, 2823–2832.
18. Tsuzuki, S.; Wakisaka, A.; Ono, T.; et al. Magnitude and Origin of the Attraction and Directionality of the Halogen Bonds of the Complexes of C_6F_5X and C_6H_5X (X = I, Br, Cl and F) with Pyridine. *Chem. Eur. J.* **2012**, *18*, 951–960.
19. Huber, S.M.; Scanlon, J.D.; Jimenez-Izal, E.; et al. On the Directionality of Halogen Bonding. *Phys. Chem. Chem. Phys.* **2013**, *15*, 10350–10357.
20. Torii, H.; Yoshida, M. Properties of Halogen Atoms for Representing Intermolecular Electrostatic Interactions Related to Halogen Bonding and Their Substituent Effects. *J. Comput. Chem.* **2010**, *31*, 107–116.
21. Torii, H. Properties of Halogen Atoms Related to the Electrostatic Origin of Halogen Bonding: Basic Aspects and Some Applications. *AIP Conf. Proc.* **2012**, *1504*, 228–239.
22. Clark, T.; Hennemann, M.; Murray, J.S.; et al. Halogen Bonding: The σ-Hole. *J. Mol. Model.* **2007**, *13*, 291–296.
23. Kolář, M.H.; Hobza, P. Computer Modeling of Halogen Bonds and Other σ-Hole Interactions. *Chem. Rev.* **2016**, *116*, 5155–5187.
24. Torii, H. The Role of Atomic Quadrupoles in Intermolecular Electrostatic Interactions of Polar and Nonpolar Molecules. *J. Chem. Phys.* **2003**, *119*, 2192–2198.
25. Jahromi, H.J.; Eskandari, K. Halogen Bonding: A Theoretical Study Based on Atomic Multipoles Derived from Quantum Theory of Atoms in Molecules. *Struct. Chem.* **2013**, *24*, 1281–1287.
26. Cardamone, S.; Hughes, T.J.; Popelier, P.L.A. Multipolar Electrostatics. *Phys. Chem. Chem. Phys.* **2014**, *16*, 10367–10387.
27. Tsuzuki, S. Origin of Attraction and Directionality of Hydrogen Bond and Halogen Bond: Analysis by ab initio MO Calculations. *AIP Conf. Proc.* **2015**, *1702*, 090044.
28. Ibrahim, M.A.A. Molecular Mechanical Study of Halogen Bonding in Drug Discovery. *J. Comput. Chem.* **2011**, *32*, 2564–2574.
29. Gutiérrez, I.S.; Lin, F.-Y.; Vanommeslaeghe, K.; et al. Parametrization of Halogen Bonds in the CHARMM General Force Field: Improved Treatment of Ligand–Protein Interactions. *Bioorg. Med. Chem.* **2016**, *24*, 4812–4825.
30. Jorgensen, W.L.; Schyman, P. Treatment of Halogen Bonding in the OPLS-AA Force Field: Application to Potent Anti-HIV Agents. *J. Chem. Theory Comput.* **2012**, *8*, 3895–3901.
31. Kolář, M.; Hobza, P. On Extension of the Current Biomolecular Empirical Force Field for the Description of Halogen Bonds. *J. Chem. Theory Comput.* **2012**, *8*, 1325–1333.
32. Nunes, R.; Vila-Viçosa, D.; Costa, P.J. Tackling Halogenated Species with PBSA: Effect of Emulating the σ-Hole. *J. Chem. Theory Comput.* **2019**, *15*, 4241–4251.
33. Saito, K.; Izumi, R.; Torii, H. Dissecting the Electric Quadrupolar and Polarization Effects Operating in Halogen Bonding through Electron Density Analysis with a Focus on Bromine. *J. Chem. Phys.* **2020**, *153*, 174302.
34. Sakai, T.; Torii, H. Substituent Effect and Its Halogen-Atom Dependence of Halogen Bonding Viewed through Electron Density Changes. *Chem. Asian J.* **2023**, *18*, e202201196.
35. Wieske, L.H.E.; Erdélyi, M. Halogen Bonds of Halogen(I) Ions─Where Are We and Where to Go? *J. Am. Chem. Soc.* **2024**, *146*, 3–18.
36. Turunen, L.; Erdélyi, M. Halogen Bonds of Halonium Ions. *Chem. Soc. Rev.* **2020**, *49*, 2688–2700.
37. Hakkert, S.B.; Erdélyi, M. Halogen Bond Symmetry: The N–X–N Bond. *J. Phys. Org. Chem.* **2015**, *28*, 226–233.
38. Carlsson, A.-C.C.; Gräfenstein, J.; Laurila, J.L.; et al. Symmetry of $[N–X–N]^+$ Halogen Bonds in Solution. *Chem. Commun.* **2012**, *48*, 1458–1460.
39. Karim, A.; Reitti, M.; Carlsson, A.-C.C.; et al. The Nature of $[N–Cl–N]^+$ and $[N–F–N]^+$ Halogen Bonds in Solution. *Chem. Sci.* **2014**, *5*, 3226–3233.
40. Pröhm, P.; Berg, W.; Rupf, S.M.; et al. On Pyridine Chloronium Cations. *Chem. Sci.* **2023**, *14*, 2325–2329.
41. Ramasami, P.; Murray, J.S. Anisotropies in Electronic Densities and Electrostatic Potentials of Halonium Ions: Focus on Chlorine, Bromine and Iodine. *J. Mol. Model.* **2024**, *30*, 81.
42. Carlsson, A.-C.C.; Gräfenstein, J.; Budnjo, A.; et al. Symmetric Halogen Bonding Is Preferred in Solution. *J. Am. Chem. Soc.* **2012**, *134*, 5706–5715.
43. Georgiou, D.C.; Butler, P.; Browne, E.C.; et al. On the Bonding in Bis-pyridine Iodonium Cations. *Aust. J. Chem.* **2013**, *66*, 1179–1188.

44. Razmazma, H.; Ebrahimi, A. The Effects of Cation-π and Anion-π Interactions on Halogen Bonds in the $[N\cdots X\cdots N]^+$ Complexes: A Comprehensive Theoretical Study. *J. Mol. Graph. Model.* **2018**, *84*, 134–144.
45. Velasquez, J.D.; Echeverría, J.; Alvarez, S. Structure and Bonding of Halonium Compounds. *Inorg. Chem.* **2023**, *62*, 8980–8992.
46. Barluenga, J.; Gonzalez, J.M.; Garcia-Martin, M.A.; et al. Acid-Mediated Reaction of Bis(Pyridine)Iodonium(I) Tetrafluoroborate with Aromatic Compounds. A Selective and General Iodination Method. *J. Org. Chem.* **1993**, *58*, 2058–2060.
47. Guha, S.; Kazi, I.; Nandy, A.; et al. Role of Lewis-Base-Coordinated Halogen(I) Intermediates in Organic Synthesis: The Journey from Unstable Intermediates to Versatile Reagents. *Eur. J. Org. Chem.* **2017**, *2017*, 5497–5518.
48. Oishi, S.; Fujinami, T.; Masui, Y.; et al. Three-Center-Four-Electron Halogen Bond Enables Non-Metallic Complex Catalysis for Mukaiyama-Mannich-Type Reaction. *iScience* **2022**, *25*, 105220.
49. Turunen, L.; Peuronen, A.; Forsblom, S.; et al. Tetrameric and Dimeric $[N\cdots I^+\cdots N]$ Halogen-Bonded Supramolecular Cages. *Chem. Eur. J.* **2017**, *23*, 11714–11718.
50. Warzok, U.; Marianski, M.; Hoffmann, W.; et al. Surprising Solvent-Induced Structural Rearrangements in Large $[N\cdots I^+\cdots N]$ Halogen-Bonded Supramolecular Capsules: An Ion Mobility-Mass Spectrometry Study. *Chem. Sci.* **2018**, *9*, 8343–8351.
51. Vanderkooy, A.; Gupta, A.K.; Földes, T.; et al. Halogen Bonding Helicates Encompassing Iodonium Cations. *Angew. Chem. Int. Ed.* **2019**, *58*, 9012–9016.
52. An, S.; Hao, A.; Xing, P. Supramolecular Axial Chirality in $[N–I–N]^+$-Type Halogen Bonded Dimers. *Chem. Sci.* **2023**, *14*, 10194–10202.
53. Haque, I.; Wood, J.L. The Vibrational Spectra and Structure of the Bis(Pyridine)Iodine(I), Bis(Pyridine)Bromine(I), Bis(γ-Picoline)Iodine(I) and Bis(γ-Picoline)Bromine(I) Cations. *J. Mol. Struct.* **1968**, *2*, 217–238.
54. Torii, H. Intermolecular Charge Flux as the Origin of Infrared Intensity Enhancement upon Halogen-Bond Formation of the Peptide Group. *J. Chem. Phys.* **2010**, *133*, 034504.
55. Torii, H. Correlation of the Partial Charge-Transfer and Covalent Nature of Halogen Bonding with the THz and IR Spectral Changes. *Phys. Chem. Chem. Phys.* **2019**, *21*, 17118–17125.
56. Ino, K.; Torii, H. Relative Importance of Electrostatic and Intermolecular Charge-Transfer Interactions in Halogen Bonding Depending on the Properties Analyzed. *Phys. Chem. Chem. Phys.* **2025**, *27*, 19295–19303.
57. Decius, J.C. An effective Atomic Charge Model for Infrared Intensities. *J. Mol. Spectrosc.* **1975**, *57*, 348–362.
58. van Straten, A.J.; Smit, W.M.A. Bond Charge Parameters from Integrated Infrared Intensities. *J. Mol. Spectrosc.* **1976**, *62*, 297–312.
59. Gussoni, M.; Castiglioni, C.; Zerbi, G. Physical Meaning of Electrooptical Parameters Derived from Infrared Intensities. *J. Phys. Chem.* **1984**, *88*, 600–604.
60. Gussoni, M.; Ramos, M.N.; Castiglioni, C.; et al. Ab Initio Counterpart of Infrared Atomic Charges: Charge Fluxes. *Chem. Phys. Lett.* **1989**, *160*, 200–205.
61. Torii, H.; Tasumi, M. Infrared Intensities of Vibrational Modes of an α-Helical Polypeptide: Calculations Based on the Equilibrium Charge/Charge Flux (ECCF) Model. *J. Mol. Struct.* **1993**, *300*, 171–179.
62. Torii, H. Cooperative Contributions of the Intermolecular Charge Fluxes and Intramolecular Polarizations in the Far-Infrared Spectral Intensities of Liquid Water. *J. Chem. Theory Comput.* **2014**, *10*, 1219–1227.
63. Corrsin, L.; Fax, B.J.; Lord, R.C. The Vibrational Spectra of Pyridine and Pyridine-d_5. *J. Chem. Phys.* **1953**, *21*, 1170–1176.
64. Partal Ureña, F.; Fernández Gómez, M.; López González, J.J.; et al. A New Insight into the Vibrational Analysis of Pyridine. *Spectrochim. Acta Part A* **2003**, *59*, 2815–2839.
65. Torii, H.; Ukawa, R. Role of Intermolecular Charge Fluxes in the Hydrogen-Bond-Induced Frequency Shifts of the OH Stretching Mode of Water. *J. Phys. Chem. B* **2021**, *125*, 1468–1475.
66. Torii, H. Roles of Electrostatics and Intermolecular Electronic Motions in the Structural and Spectroscopic Features of Hydrogen- and Halogen-Bonded Systems. *Pure Appl. Chem.* **2024**, *96*, 579–595.
67. Chai, J.-D.; Head-Gordon, M. Long-Range Corrected Hybrid Density Functionals with Damped Atom–Atom Dispersion Corrections. *Phys. Chem. Chem. Phys.* **2008**, *10*, 6615–6620.
68. Weigend, F.; Ahlrichs, R. Balanced Basis Sets of Split Valence, Triple Zeta Valence and Quadruple Zeta Valence Quality for H to Rn: Design and Assessment of Accuracy. *Phys. Chem. Chem. Phys.* **2005**, *7*, 3297–3305.
69. Weigend, F. Accurate Coulomb-fitting Basis Sets for H to Rn. *Phys. Chem. Chem. Phys.* **2006**, *8*, 1057–1065.
70. Del Bene, J.E.; Elguero, J. Systematic ab Initio Study of $^{15}N–^{15}N$ and $^{15}N–^{1}H$ Spin−Spin Coupling Constants Across $N–H^+–N$ Hydrogen Bonds: Predicting N−N and N−H Coupling Constants and Relating Them to Hydrogen Bond Type. *J. Phys. Chem. A* **2006**, *110*, 7496–7502.
71. Tayyari, S.F.; Mahdizadeh, S.J.; Holakoei, S.; et al. Vibrational Assignment and Proton Tunneling in Pyridine–Pyridinium Complexes. *J. Mol. Struct.* **2010**, *971*, 39–46.

72. Melikova, S.M.; Rutkowski, K.S.; Gurinov, A.A.; et al. FTIR Study of the Hydrogen Bond Symmetry in Protonated Homodimers of Pyridine and Collidine in Solution. *J. Mol. Struct.* **2012**, *1018*, 39–44.
73. Attah, I.K.; Platt, S.P.; Meot-Ner (Mautner), M.; et al. Proton-Bound Dimers of Nitrogen Heterocyclic Molecules: Substituent Effects on the Structures and Binding Energies of Homodimers of Diazine, Triazine, and Fluoropyridine. *J. Chem. Phys.* **2014**, *140*, 114313.
74. Frisch, M.J.; Trucks, G.W.; Schlegel, H.B.; et al. *Gaussian 09, Revision D.01*; Gaussian, Inc.: Wallingford, CT, USA, 2013.
75. Agmon, N.; Bakker, H.J.; Campen, R.K.; et al. Protons and Hydroxide Ions in Aqueous Systems. *Chem. Rev.* **2016**, *116*, 7642–7672.
76. Biswas, R.; Carpenter, W.; Fournier, J.A.; et al. IR Spectral Assignments for the Hydrated Excess Proton in Liquid Water. *J. Chem. Phys.* **2017**, *146*, 154507.
77. Zundel, G. Hydration Structure and Intermolecular Interaction in Polyelectrolytes. *Angew. Chem. Int. Ed.* **1969**, *8*, 499–509.